



Article

# A Two-Step Synthesis of Porous Nitrogen-Doped Graphene for Electrochemical Capacitors

Jiahao Li , Zhenjia Wu, Rong Huang, Anbang Ge and Jie Ying \*

School of Chemical Engineering and Technology, Sun Yat-sen University, Zhuhai 519082, China; lijh255@mail2.sysu.edu.cn (J.L.); wuzhj58@mail2.sysu.edu.cn (Z.W.); huangr279@mail2.sysu.edu.cn (R.H.); geanb@mail2.sysu.edu.cn (A.G.)

\* Correspondence: yingj5@mail.sysu.edu.cn

**Abstract:** Porous nitrogen-doped graphene (PNG) materials with high conductivity, high surface area, and chemical stability have displayed superior performance in electrochemical capacitors. However, previously reported methods for fabricating PNG render the processes expensive, hard to control, limited in production, and unsafe as well, thus largely restricting their practical applications. Herein, we present a facile two-step calcination method to prepare PNG using petroleum asphalt as the carbon source to provide the original three-dimensional porous structure directly and using environmentally friendly and high nitrogen content urea as the nitrogen source without adding any etching agent. The porous structure in PNG can largely increase its specific surface area, and the introduction of nitrogen atoms can effectively increase the degree of defects and improve the wettability of PNG. As a result, PNG displays a high specific capacitance of  $157 \text{ F g}^{-1}$  at a current density of  $1 \text{ A g}^{-1}$  and cycling stability while maintaining 98.68% initial capacitance after 10,000 cycles.

**Keywords:** porous nitrogen-doped graphene; petroleum asphalt; electrochemical capacitors



**Citation:** Li, J.; Wu, Z.; Huang, R.; Ge, A.; Ying, J. A Two-Step Synthesis of Porous Nitrogen-Doped Graphene for Electrochemical Capacitors. *Int. J. Mol. Sci.* **2024**, *25*, 12297. <https://doi.org/10.3390/ijms252212297>

Academic Editor: Giovanna Iezzi

Received: 19 October 2024

Revised: 11 November 2024

Accepted: 14 November 2024

Published: 15 November 2024



**Copyright:** © 2024 by the authors. Licensee MDPI, Basel, Switzerland. This article is an open access article distributed under the terms and conditions of the Creative Commons Attribution (CC BY) license (<https://creativecommons.org/licenses/by/4.0/>).

## 1. Introduction

The development of high-power-density storage devices is regarded as indispensable because of the booming market of mobile and immobile electronic devices [1–3]. Electrochemical capacitors, otherwise known as supercapacitors, which offer high power density, long cycle life, and rapid charge–discharge capacity, have attracted extensive attention [4–7]. It is widely recognized that the performance of electrochemical capacitors is mainly decided by the electrode materials. Thus, the design and fabrication of high-performance electrode materials can contribute to enhancing the properties of electrochemical capacitors. Recently, a series of carbon materials with high conductivity has been investigated as efficient electrode materials for electrochemical capacitors [8–13]. Among them, porous nitrogen-doped graphene (PNG) materials display high surface area and chemical stability and thus have high electrochemical performance such as capacitance, rate capability, and cycling stability [14–19].

At present, PNG can be produced either using graphene oxide through self-assembly [20–22] and 3D printing [23–25] or by way of chemical vapor deposition [26–28]. In these configurations, pores are created between nanosheets by means of cross-linking gelation or a template drive, endowing the graphene frameworks with diverse structures and multiple functions. Moreover, it has been confirmed that introducing heteroatom dopants such as nitrogen into graphene can further modulate their electronic properties and electrochemical performance [15,29,30]. However, these methods for manufacturing PNG render the processes expensive, hard to control, limited in production, and unsafe as well, thus severely restricting their practical applications [31,32]. Therefore, the development of a simple, low-cost, and environmentally friendly approach for the fabrication of PNG is of considerable significance.

As a low-value by-product in petroleum processing, petroleum asphalt has attracted much attention because of its low cost and large quantity (over 25 million tons per year) [19,33].

The content of polycyclic aromatic hydrocarbons in petroleum asphalt is rich, and the content of ash is low, so the carbon material produced by carbonization has excellent porosity and ideal electrical conductivity [34,35]. Herein, we report the fabrication of PNG through a two-step calcination method using petroleum asphalt as a carbon source and urea as a nitrogen source without adding any etching agent. The porous structure effectively increases the specific surface area of PNG and promotes the transfer of electrolytic ions. In addition, the introduction of nitrogen atoms increases the degree of defects and improves the wettability of the material. Benefiting from this, PNG has superior specific capacitance and cycle stability, proving its good electrochemical properties as an electrode material for electrochemical capacitors.

## 2. Results and Discussion

The overall synthetic procedure of PNG- $x$  ( $x$  represents the amount of urea added) is displayed in Figure 1. Asphalt, urea, and mixed salt are oxidized in the air after ball milling, and the unstable components in the mixture are decomposed into  $\text{CO}_2$  and  $\text{CO}$  gas molecules, thus obtaining pre-PNG with mesoporous and macroporous. After high-temperature carbonization, the cross-linked oxygen-containing functional groups between the carbon layers can be removed, thereby expanding the carbon layer spacing. Then the mixed salt is removed with deionizing water, and finally, PNG- $x$  is obtained.

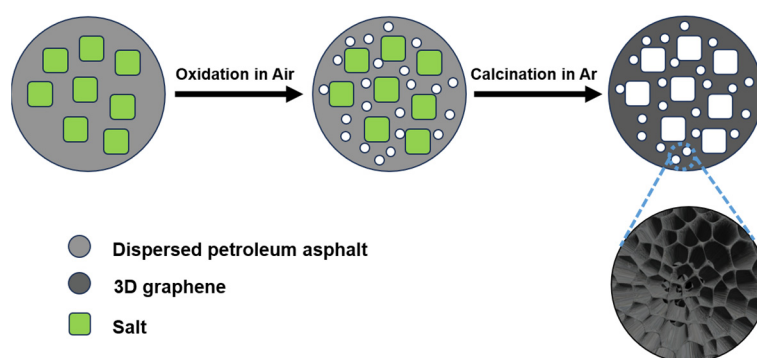


**Figure 1.** Scheme illustration of synthesis of PNG- $x$ .

The morphologies of PNG- $x$  are shown in Figure 2a–f. It can be seen that PNG- $x$  has an obvious porous network structure, and with the increase in urea content, the morphology of PNG- $x$  still maintains a porous structure. This proves that the two-step oxidation carbonization method can be effectively applied to the production of porous structures. In order to further confirm the mesostructure and element distribution of PNG- $x$ , PNG-0.6 is characterized by transmission electron microscopy (TEM). Figure 3a,b are TEM images of PNG-0.6 at different magnifications. As can be seen from Figure 3a, PNG-0.6 has a clear three-dimensional porous structure. In addition, the lamellar surface of PNG-0.6 is rich in mesoporous pores (Figure 3b). Figure 3c presents the high-angle annular dark-field scanning TEM (HAADF-STEM) image of a part of PNG-0.6, and the corresponding elemental mapping images in Figure 3d–f indicate that the elements C, N, and O are homogeneously distributed throughout PNG-0.6, revealing that nitrogen obtained from urea decomposition can be effectively doped into graphene. It is worth noting that the three-dimensional porous structure of PNG- $x$  has little effect on wettability, and PNG- $x$  exhibits hydrophobicity only at suitable nitrogen doping levels (Figure 3g). Among them, PNG-0.6 exhibits hydrophobicity, which can avoid the adsorption of water and minimize the impact of water on the performance of the capacitor [36].

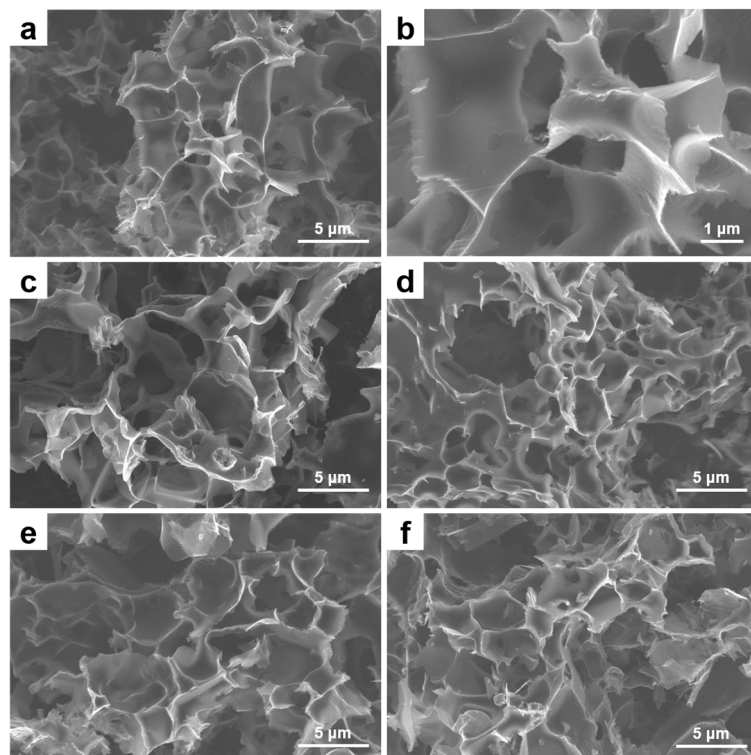


**Figure 2.** SEM images of (a,b) PNG-0.6, (c) PNG-0, (d) PNG-1.2, (e) PNG-1.5, (f) PNG-2.0.

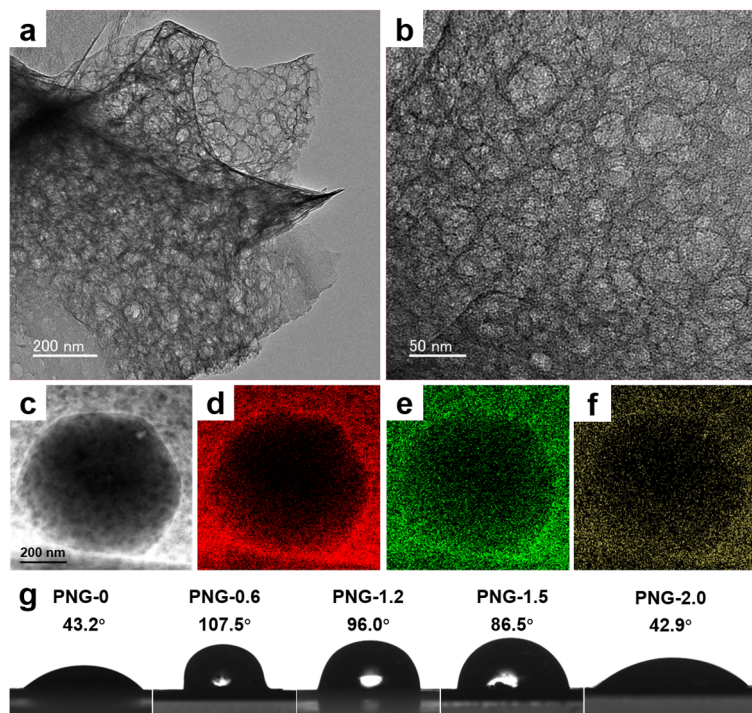


**Figure 3.** (a,b) TEM images of PNG-0.6, (c) HAADF-STEM images of PNG-0.6, (d–f) EDS elemental mappings of C, N, and O, (g) water drops on PNG-x.

The crystalline structure of all the samples is determined using X-ray diffraction (XRD) (Figure 4a). For all samples, two broad peaks can be observed on the XRD pattern, corresponding to the (002) and (100) crystal faces of the carbon material [18,37,38]. The diffraction angle  $2\theta$  of PNG-0.6 at the (002) plane is around  $24.4^\circ$ , and the average layer spacing of PNG-0.6 can be calculated as 0.358 nm according to the Bragg equation. With

the increase in urea content, the diffraction peak of PNG-x at (002) plane gradually moves to the higher angle, which proves that the increase in urea content will reduce the layer spacing of PNG-x.

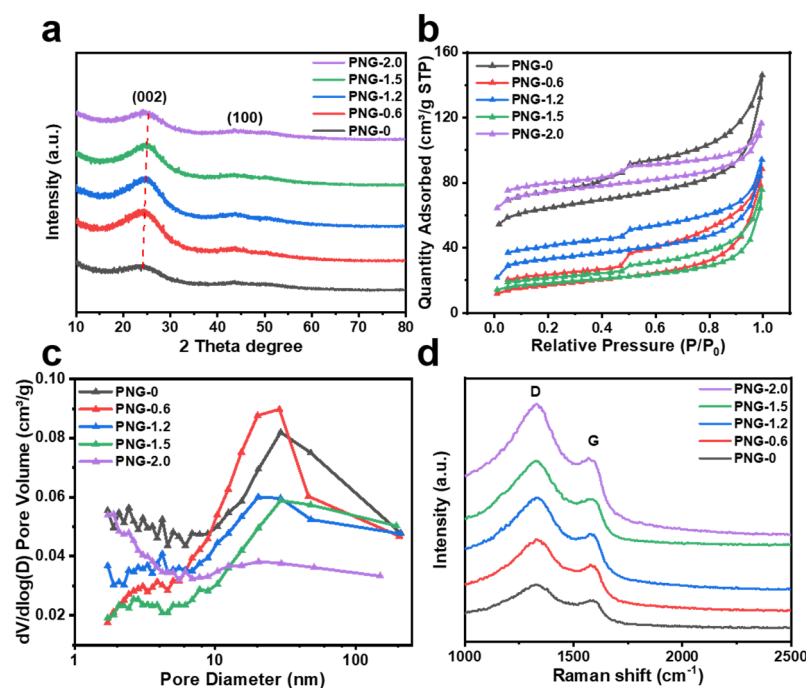


**Figure 4.** (a) XRD patterns of PNG-x, (b)  $N_2$  adsorption and desorption isotherm curves of PNG-x, (c) diameter distribution curves of PNG-x, (d) Raman spectra of PNG-x.

The nitrogen adsorption/desorption isotherms of the samples are shown in Figure 4b. A typical type IV isotherm characteristic accompanied by a hysteresis loop is observed, indicating that there are a large number of mesopores in PNG-x [39,40]. As indicated in Table 1, the specific surface areas of the PNG-0, PNG-0.6, PNG-1.2, PNG-1.5, and PNG-2.0 samples, which are calculated based on the Brunauer–Emmett–Teller (BET) method, are 242, 61, 128, 67, and 283  $m^2 g^{-1}$  respectively. The pore volumes are 0.226, 0.137, 0.146, 0.117, and 0.180  $cm^3 g^{-1}$ , respectively. The pore size of PNG-x calculated using the Barrett–Joyner–Halenda (BJH) method is mainly distributed in the mesoporous region (Figure 4c). In addition, the results in Table 1 show that adding a small amount of urea can significantly reduce the content of micropores, leading to a decrease in surface area and pore volume. With the increase in urea content, the micropore content gradually increases, and the surface area and pore volume of PNG-x will increase significantly.

**Table 1.** Specific surface area and pore volume of PNG-x.

Sample	$S_{BET}^a$ $m^2 g^{-1}$	$V_t^b$ $cm^3 g^{-1}$	$V_m^c$ $cm^3 g^{-1}$
PNG-0	242	0.226	0.083
PNG-0.6	61	0.137	0.011
PNG-1.2	128	0.146	0.038
PNG-1.5	67	0.117	0.018
PNG-2.0	283	0.180	0.105

<sup>a</sup> BET-specific surface area; <sup>b</sup> total pore volume from adsorption isotherms at a relative pressure  $P/P_0$  of 0.99; <sup>c</sup> t-plot micropore volume.

Raman spectroscopy is a unique, non-destructive technique to investigate the structure properties of carbon materials. Figure 4d is the Raman spectrogram of PNG-x, from which peak D near  $1330 cm^{-1}$  and peak G near  $1570 cm^{-1}$  are observed. As shown in Table 2, the

$I_D/I_G$  ratio of PNG-x gradually increased with the increase in urea content. The higher the  $I_D/I_G$  ratio, the higher the defect degree of PNG-x and the lower the graphitization degree, indicating that the incorporation of nitrogen atoms provided defect sites [41–43]. Moreover, the  $I_D/I_G$  ratio of PNG-x supplemented with urea is all greater than PNG-0 (1.08), which is largely due to the destruction of local symmetry by nitrogen atom doping, resulting in an increase in D-band intensity.

**Table 2.**  $I_D/I_G$  of PNG-x.

Sample	$I_D/I_G$ <sup>a</sup>
PNG-0	1.08
PNG-0.6	1.13
PNG-1.2	1.17
PNG-1.5	1.19
PNG-2.0	1.23

<sup>a</sup> The intense ratio of D band and G band from Raman spectra.

X-ray photoelectron spectroscopy (XPS) is further employed to analyze the surface compositions of PNG-x. The full XPS spectra in Figure 5a clarified that all the PNG-x are composed of C, N, and O. The N 1s high-resolution peak of the PNG-0.6 in Figure 5b can be modeled into four independent peaks of 389.4 eV, 400.1 eV, 401.1 eV, and 403.1 eV, corresponding to the characteristic peaks of pyridinic-N (N-6), pyrrolic-N (N-5), graphitic-N (N-Q), and oxidized-N (N-X), respectively [44–48]. In addition, the N 1s high-resolution spectra of other samples, as shown in Figure 5c–f, can be convolved into four peaks of N-6, N-5, N-Q, and N-x. The nitrogen content of PNG-x increased from 4.18 at% to 8.96 at% with the increase in urea content (Table 3). Meanwhile, with the increase in defect nitrogen content (PNG-0 < PNG-0.6 < PNG-1.5 < PNG-1.2 < PNG-2.0), the specific surface area of PNG decreases first and then increases. This may be because the three-dimensional porous structure of PNG is first partially destroyed with the increase in urea, resulting in a decrease in the specific surface area. Then, the urea content continues to increase, which forms part of the porous carbon material, resulting in an increase in the specific surface area. Supercapacitors are classified into electrical double-layer capacitors and pseudocapacitors based on their charge storage mechanisms [49]. Among these nitrogen functional groups, N-6 and N-5 are thought to contribute more to specific capacitors by introducing pseudocapacitors, while N-Q can effectively improve the conductivity of carbon materials by promoting electron transfer, which means that PNG-0.6 has good supercapacitor performance [14].

**Table 3.** Nitrogen content (at%) and nitrogen binding state in PNG-x obtained by XPS.

Sample	The Ratio of Different N Groups (at%)				
	Total	Pyridinic-N	Pyrrolic-N	Graphitic-N	Oxidized-N
PNG-0	4.18	1.63	0.85	0.96	0.74
PNG-0.6	5.44	1.20	1.63	1.28	1.33
PNG-1.2	8.05	3.68	0.97	2.53	0.87
PNG-1.5	8.42	3.14	0.76	2.55	1.97
PNG-2.0	8.96	3.65	1.06	2.48	1.77

The electrochemical properties of PNG-x samples were examined in an alkaline medium. As shown in Figure 6a, cyclic voltammetry (CV) curves of different samples at a scanning rate of 100 mV s<sup>−1</sup> are presented. All samples showed an approximate spindle shape, indicating the existence of electric double-layer capacitors. It is worth noting that PNG-0.6 has the largest total area. It is widely known that the specific capacitance is in proportion to the area of the CV curve, thus indicating that less nitrogen doping will increase the overall capacitance.

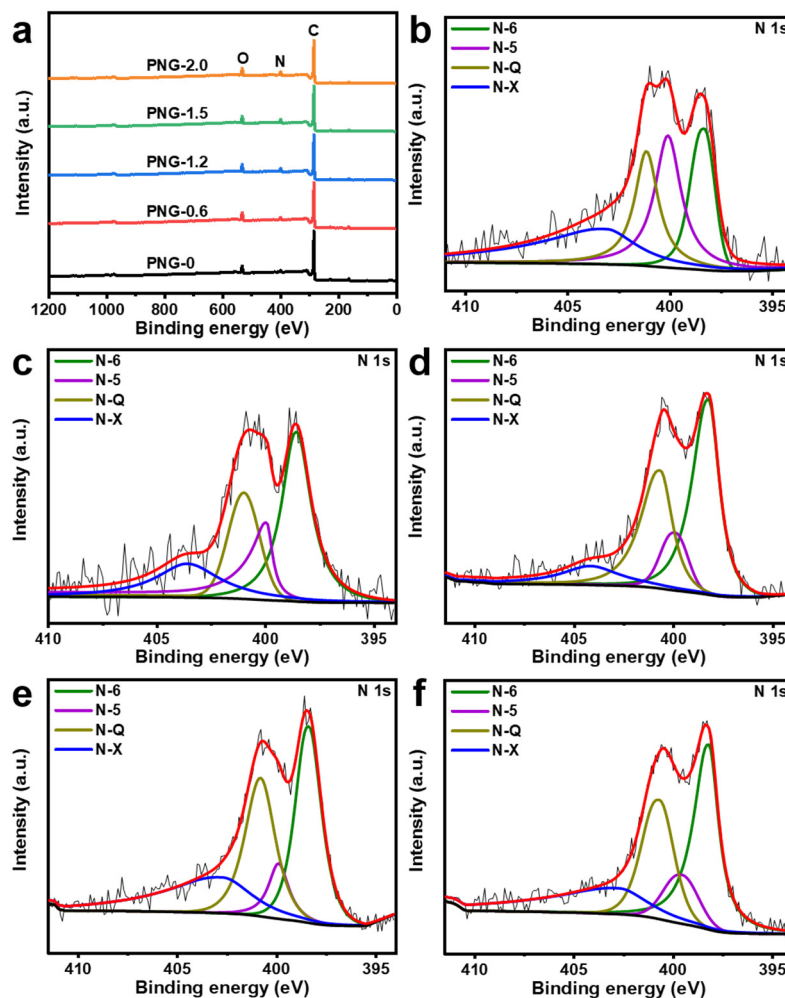


**Figure 5.** (a) XPS survey spectra of PNG-x, XPS high-resolution N 1s spectra of (b) PNG-0.6, (c) PNG-0, (d) PNG-1.2, (e) PNG-1.6, and (f) PNG-2.0.

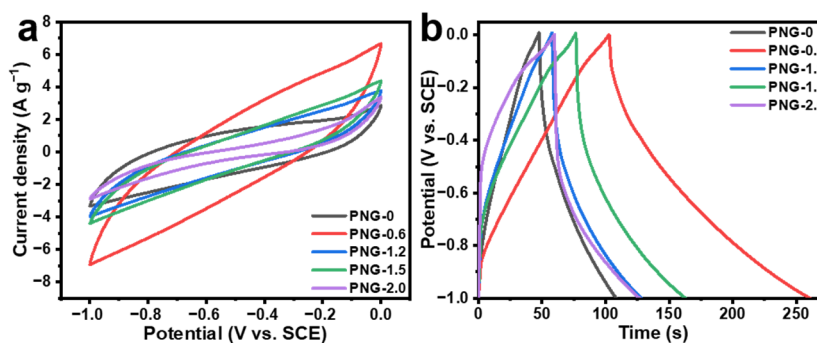


**Figure 6.** (a) CV curves of PNG-x at  $100 \text{ mV s}^{-1}$ , (b) GCD curves of PNG-x at  $1 \text{ A g}^{-1}$ .

The specific capacitance values of the PNG-x computed from galvanostatic charge–discharge (GCD) curves (refer to Figure 6b) were  $60 \text{ F g}^{-1}$  (PNG-0),  $157 \text{ F g}^{-1}$  (PNG-0.6),  $69 \text{ F g}^{-1}$  (PNG-1.2),  $89 \text{ F g}^{-1}$  (PNG-1.5), and  $66 \text{ F g}^{-1}$  (PNG-2.0), respectively. It can be seen that the nitrogen-doped sample has a higher specific capacitance than the sample without urea. PNG-0.6 has a high specific capacitance mainly for the following two reasons: (1) pyridinic-N and pyrrolic-N can enhance electrochemical reactivity, and (2) the rich pore structure is beneficial for improving the contact area between the electrode and the electrolyte and reducing the resistance to transfer of electrolytic ions [50,51]. Although the surface area of PNG-1.2 and PNG-2.0 is much larger than that of PNG-0.6, their high

nitrogen doping actually hinders electron transfer and reduces capacitance. PNG-1.5 also has a lower surface area than PNG-0.6, lacking enough space to transfer electrolytic ions.

Figure 7a presents the CV curves of the PNG-0.6 at different scan rates varying from 10 to 300  $\text{mV s}^{-1}$ . With the increase in the scan rate, the CV loop maintains its spindle shape, suggesting that very little polarization occurs because of the high electronic conductivity of PNG-0.6. The GCD curves of PNG-0.6 are shown in Figure 7b. The curves are nearly triangular in shape, featuring slight curvature and no obvious potential drop at a current density ranging from 0.5 and 5  $\text{A g}^{-1}$ , which indicates its outstanding electrochemical reversibility and rapid I–V response. Figure 7c plots the relationship between specific capacitance and current density of PNG-0.6. As the current density increases, the specific capacitance gradually decreases, which might be attributed to the limited diffusion of electrolyte ions. In addition, when the current density rises from 1  $\text{A g}^{-1}$  to 5  $\text{A g}^{-1}$ , about 34% of the specific capacitance scale remains unchanged, indicating that PNG-0.6 has excellent rate capability for electrochemical capacitors. This may be related to the porous structure and excellent electronic conductivity of PNG-0.6 [52].

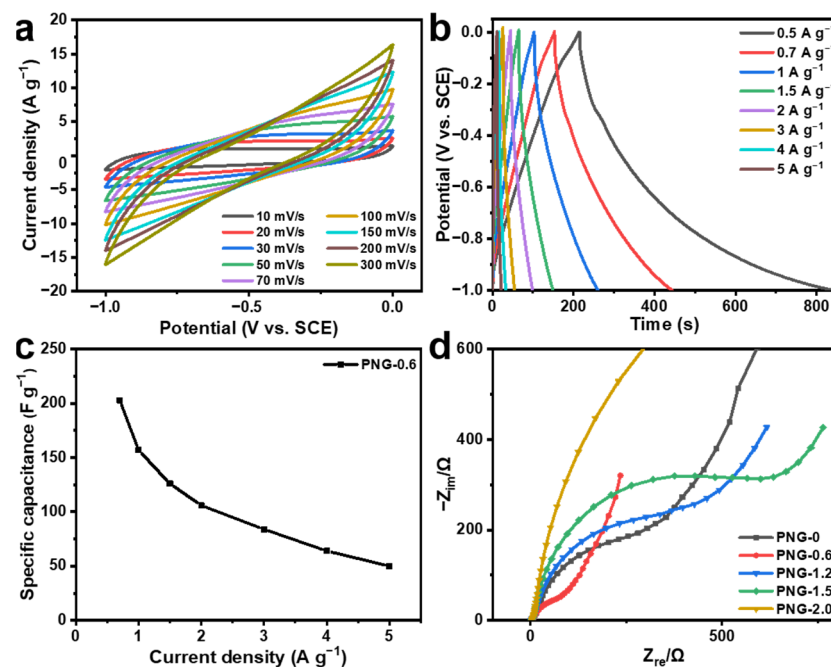


**Figure 7.** (a) CV curves at different scan rates for the PNG-0.6. (b) GCD curves at different current densities for PNG-0.6, (c) the specific capacitance versus current density for PNG-0.6, (d) Nyquist plots of PNG-x.

To further explore the electrochemical behavior of the PNG-x sample, electrochemical impedance spectroscopy (EIS) tests were carried out at an open-circuit voltage in the frequency range from  $10^{-2}$  Hz to  $10^5$  Hz. As shown in Figure 7d, all samples except PNG-2.0 exhibit vertical slopes in the low-frequency region, suggesting that the sample has good capacitance and low ion diffusion resistivity at the electrode/electrolyte interface. Moreover, the charge transfer impedance of PNG-0.6 is considerably lower than that of other samples, indicating that proper nitrogen doping can efficiently enhance the electrochemical properties of the material. However, too much nitrogen atom doping will lead to a decrease in resistivity and not enough to achieve fast charge transfer kinetics.

Cycling stability performance is a highly significant parameter for electrochemical capacitors. As demonstrated in Figure 8a, after 1000 cycles, the specific capacitance of PNG-0.6 began to increase, reaching a maximum of 99.92% of the initial specific capacity (3000 cycles). It may be that during the cycle, some of the graphitized carbon in PNG-0.6 degenerates to a more disordered degree, exposing more active sites and thus contributing to better contact between the electrode and the electrolyte [53]. And after 10,000 cycles, it

can still retain 98.68% of the initial specific capacitance. The results show that PNG-0.6 has excellent cyclic stability. Moreover, the first, the 2000th, 4000th, 6000th, 8000th, and 10,000th CV curves of PNG-0.6 obtained at  $200 \text{ mV}^{-1}$  are shown in Figure 8b. The CV curves are almost identical, which further indicates that PNG-0.6 is an excellent and stable electrochemical electrode material.

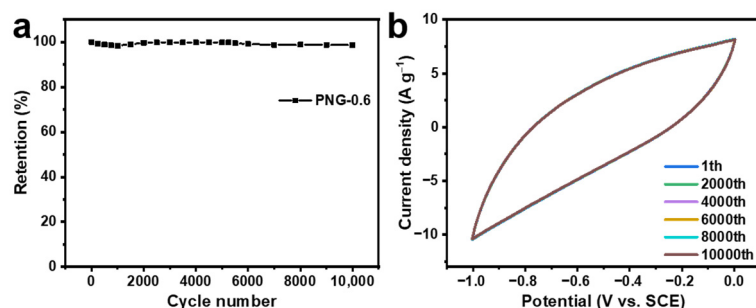


**Figure 8.** (a) Cycling stability of PNG-0.6, (b) The first, 2000th, 4000th, 6000th, 8000th, 10,000th CV curves of the PNG-0.6 at  $200 \text{ mV s}^{-1}$ .

### 3. Materials and Methods

#### 3.1. Materials

Petroleum asphalt was purchased from Wentian New Materials Tech. Co., Ltd., Huizhou, China. Liquid aromatic petrochemical by-products were purchased from China Railway Weiye Waterproof Material Technology Co., Ltd., Jinan, China. Urea ( $\text{CH}_4\text{N}_2\text{O}$ ), sodium chloride (NaCl), potassium chloride (KCl), and potassium hydroxide (KOH) were purchased from Aladdin Industrial Corporation, Shanghai, China. Nafion (5 wt%) was purchased from Sigma-Aldrich, Shanghai, China.

#### 3.2. Synthesis of PNG-*x*

PNG-*x* was synthesized by a two-step oxidation carbonization process. In a typical procedure, 1 g petroleum asphalt was dispersed with 10 mL liquid aromatic petrochemical by-products by ultrasonic for 20 min. The above mixture was ball-milled with 20 g NaCl:KCl (mass ratio 4.5:5.5) and *x* (*x* = 0, 0.6, 1.2, 1.5, 2.0) g urea to obtain a homogeneous solid mixture. Next, the mixture was heated at a heating rate of  $5 \text{ }^\circ\text{C min}^{-1}$  to  $300 \text{ }^\circ\text{C}$  in a muffle furnace under air atmosphere and maintained for 2 h to obtain pre-PNG. Then, the sample was calcined at a heating rate of  $3 \text{ }^\circ\text{C min}^{-1}$  to  $700 \text{ }^\circ\text{C}$  under Ar atmosphere and maintained for 2 h, after which the sample was naturally cooled to room temperature. Finally, after washing and drying, PNG-*x* was obtained.

#### 3.3. Characterization

Field-emission scanning electron microscopy (FESEM) was conducted on ThermoScientific Apreo 2S HiVac (Waltham, MA, USA) at the acceleration voltage of 5 kV, and TEM studies were carried out on JEOL JEM-F200 (Tokyo Japan) at the acceleration voltage of 200 kV. XRD measurements were carried out on an Ultima IV X-ray diffractometer (Tokyo, Japan) using Cu  $\text{K}\alpha$  radiation ( $\lambda = 1.54056 \text{ \AA}$ ) with a step width of  $0.05^\circ$  and step time of 0.5. The specific surface area for BET measurements was conducted using a Micromeritics ASAP 2460 system (Norcross, GA, USA). The pore size distribution of each sample was computed from the adsorption isotherm branch using the BJH method. Raman analysis was performed with a confocal Raman microscope (CRM) (Alpha300R, WITec GmbH, Ulm, Germany) equipped with a TEM single-frequency laser ( $\lambda = 633\text{nm}$ , laser power = 2 mW, WITec GmbH, Ulm, Germany). The laser light was focused through a  $50\times$  oil immersion objective onto the sample, and the backscattered Raman signal was directed through an optic multifiber ( $50 \mu\text{m}$  diameter) to a spectrometer ( $300 \text{ g}\cdot\text{mm}^{-1}$  grating) and detected by the CCD camera. On the selected areas on the sample every  $0.5 \mu\text{m}$  a full wavenumber range ( $50\text{--}2940 \text{ cm}^{-1}$ ) Raman spectrum was acquired with an integration time of 300 s. XPS



analysis was conducted on a Thermo Scientific K-Alpha X-ray photoelectron spectrometer (Waltham, MA, USA). The N 1s spectra were acquired at photon energy (h $\nu$ ) of 1486.6 eV and analyzer pass energies (PE) of 50 eV. The survey spectra were acquired at photon energy (h $\nu$ ) of 1486.6 eV and analyzer pass energies (PE) of 150 eV.

### 3.4. Electrochemical Measurements

Electrochemical measurements were performed on Metrohm Autolab (Herisau, Switzerland) PGSTAT 302N using a three-electrode cell. A platinum foil of 4 cm<sup>2</sup> was employed as a counter electrode, and a saturated calomel electrode (SCE) was utilized as a reference electrode. The slurry-coated nickel foam was used as the working electrode. To prepare the slurry, 10 mg PNG-x and 1 mg acetylene black were dispersed in a mixed solution containing 950  $\mu$ L isopropanol and 50  $\mu$ L nafion solution (5 wt%) under ultrasonic treatment for 30 min. In total, 100  $\mu$ L of the aforementioned mixture was dropped onto nickel foam, and the coated area was approximately 1 cm  $\times$  1 cm. Subsequently, the nickel foam was left to dry overnight in the air. The mass loading of PNG-x on the nickel foam was maintained at 1 mg. All the electrochemical measurements, including CV, GCD, and EIS, were performed in 1 M KOH solution at room temperature. Generally, the CV tests were conducted at a scan rate ranging from 10 to 150 mV s<sup>-1</sup> within a potential window of -1.0 V to 0 V (versus SCE). Meanwhile, the GCD measurements were performed at a current density ranging from 0.5 to 5 A g<sup>-1</sup> with a potential window of -1.0 V to 0 V (versus SCE). The specific capacitance of all the samples can be acquired by computing from GCD curves in accordance with the following equation:

$$C_s = \frac{\Delta t \times I}{\Delta V \times m}$$

where  $C_s$ ,  $\Delta t$ ,  $I$ ,  $\Delta V$ , and  $m$  represent the specific capacitance, the discharge time, the discharge current, the potential charge during discharge, and the mass of the PNG-x, respectively.

## 4. Conclusions

In summary, a three-dimensional porous nitrogen-doped graphene with a macro-mesoporous structure has been successfully prepared by a facile two-step calcination strategy. The macro-mesoporous structure can effectively promote the transfer of electrolytic ions. Moreover, the incorporation of nitrogen atoms also boosts the electrochemical properties of the materials. Notably, PNG-0.6 has a specific capacitance of 157 F g<sup>-1</sup> when the current density is 1 A g<sup>-1</sup>, which is significantly higher than that of the other samples. The initial capacitance of 98.68% can be maintained after 10,000 CV cycles, indicating that PNG-0.6 is a promising electrochemical material. Our approach provides an opportunity to design novel porous materials with low cost, high capacitance, and long-term stability in the electrochemistry field.

**Author Contributions:** Conceptualization, J.Y.; validation, Z.W., R.H. and A.G.; investigation, Z.W., R.H., A.G. and J.L.; data curation, J.L.; writing—original draft preparation, J.L.; writing—review and editing, J.Y.; supervision, J.Y.; project administration, J.Y.; funding acquisition, J.Y. All authors have read and agreed to the published version of the manuscript.

**Funding:** This research was supported by the Program Fund of Non-Metallic Excellence and Innovation Center for Building Materials (2023TDA1-1), the National Natural Science Foundation of China (52201286), and the Guangdong Basic and Applied Basic Research Foundation (2022A1515011905, 2024A1515012613).

**Institutional Review Board Statement:** Not applicable.

**Informed Consent Statement:** Not applicable.

**Data Availability Statement:** The original contributions presented in this study are included in the article. Further inquiries can be directed to the corresponding author.

**Conflicts of Interest:** The authors declare no conflicts of interest.

## References

1. Beidaghi, M.; Wang, C. Micro-Supercapacitors Based on Interdigital Electrodes of Reduced Graphene Oxide and Carbon Nanotube Composites with Ultrahigh Power Handling Performance. *Adv. Funct. Mater.* **2012**, *22*, 4501–4510. [[CrossRef](#)]
2. Hwang, J.Y.; Li, M.; El-Kady, M.F.; Kaner, R.B. Next-Generation Activated Carbon Supercapacitors: A Simple Step in Electrode Processing Leads to Remarkable Gains in Energy Density. *Adv. Funct. Mater.* **2017**, *27*, e1605745. [[CrossRef](#)]
3. Pech, D.; Brunet, M.; Durou, H.; Huang, P.; Mochalin, V.; Gogotsi, Y.; Taberna, P.L.; Simon, P. Ultrahigh-power micrometre-sized supercapacitors based on onion-like carbon. *Nat. Nanotechnol.* **2010**, *5*, 651–654. [[CrossRef](#)]
4. Niu, L.; Wu, T.; Chen, M.; Yang, L.; Yang, J.; Wang, Z.; Kornyshev, A.A.; Jiang, H.; Bi, S.; Feng, G. Conductive Metal-Organic Frameworks for Supercapacitors. *Adv. Mater.* **2022**, *34*, e2200999. [[CrossRef](#)]
5. Wang, F.; Wu, X.; Yuan, X.; Liu, Z.; Zhang, Y.; Fu, L.; Zhu, Y.; Zhou, Q.; Wu, Y.; Huang, W. Latest advances in supercapacitors: From new electrode materials to novel device designs. *Chem. Soc. Rev.* **2017**, *46*, 6816–6854. [[CrossRef](#)] [[PubMed](#)]
6. Wang, G.; Zhang, L.; Zhang, J. A review of electrode materials for electrochemical supercapacitors. *Chem. Soc. Rev.* **2012**, *41*, 797–828. [[CrossRef](#)]
7. Yang, L.; Guo, X.; Jin, Z.; Guo, W.; Duan, G.; Liu, X.; Li, Y. Emergence of melanin-inspired supercapacitors. *Nano Today* **2021**, *37*, 101075. [[CrossRef](#)]
8. Chi, F.; Li, C.; Zhou, Q.; Zhang, M.; Chen, J.; Yu, X.; Shi, G. Graphene-Based Organic Electrochemical Capacitors for AC Line Filtering. *Adv. Energy Mater.* **2017**, *7*, 1700591. [[CrossRef](#)]
9. Guo, C.; Zhang, Y.; Zeng, T.; Huang, D.; Wan, Q.; Yang, N. High-performance asymmetric supercapacitors using holey graphene electrodes and redox electrolytes. *Carbon* **2020**, *157*, 298–307. [[CrossRef](#)]
10. Heo, Y.J.; Lee, J.W.; Son, Y.R.; Lee, J.H.; Yeo, C.S.; Lam, T.D.; Park, S.Y.; Park, S.J.; Sinh, L.H.; Shin, M.K. Large-Scale Conductive Yarns Based on Twistable Korean Traditional Paper (Hanji) for Supercapacitor Applications: Toward High-Performance Paper Supercapacitors. *Adv. Energy Mater.* **2018**, *8*, e1801854. [[CrossRef](#)]
11. Jiang, T.; Wang, Y.; Chen, G.Z. Electrochemistry of Titanium Carbide MXenes in Supercapacitor. *Small Methods* **2023**, *7*, e2201724. [[CrossRef](#)] [[PubMed](#)]
12. Liu, H.H.; Zhang, H.L.; Xu, H.B.; Lou, T.P.; Sui, Z.T.; Zhang, Y. In situ self-sacrificed template synthesis of vanadium nitride/nitrogen-doped graphene nanocomposites for electrochemical capacitors. *Nanoscale* **2018**, *10*, 5246–5253. [[CrossRef](#)] [[PubMed](#)]
13. Sahoo, G.; Polaki, S.R.; Ghosh, S.; Krishna, N.G.; Kamruddin, M.; Ostrikov, K. Plasma-tuneable oxygen functionalization of vertical graphenes enhance electrochemical capacitor performance. *Energy Storage Mater.* **2018**, *14*, 297–305. [[CrossRef](#)]
14. Liu, Z.; Qin, A.; Zhang, K.; Lian, P.; Yin, X.; Tan, H. Design and structure of nitrogen and oxygen co-doped carbon spheres with wrinkled nanocages as active material for supercapacitor application. *Nano Energy* **2021**, *90*, 106540. [[CrossRef](#)]
15. Sedajova, V.; Bakandritsos, A.; Blonski, P.; Medved, M.; Langer, R.; Zaoralova, D.; Ugolotti, J.; Dzibelova, J.; Jakubec, P.; Kupka, V.; et al. Nitrogen doped graphene with diamond-like bonds achieves unprecedented energy density at high power in a symmetric sustainable supercapacitor. *Energy Environ. Sci.* **2022**, *15*, 740–748. [[CrossRef](#)]
16. Wei, W.; Chen, Z.; Zhang, Y.; Chen, J.; Wan, L.; Du, C.; Xie, M.; Guo, X. Full-faradaic-active nitrogen species doping enables high-energy-density carbon-based supercapacitor. *J. Energy Chem.* **2020**, *48*, 277–284. [[CrossRef](#)]
17. Zhou, Q.; Chen, Q.; Xu, W.; Wang, F.; Du, X.; Zhou, Y.; Zhan, Y.; Jiang, M. Nitrogen and sulfur co-doped carbonized lignin nanotubes for supercapacitor applications. *Chem. Eng. J.* **2024**, *496*, 154126. [[CrossRef](#)]
18. Yalovega, G.E.; Brzhezinskaya, M.; Dmitriev, V.O.; Shmatko, V.A.; Ershov, I.V.; Ulyankina, A.A.; Chernysheva, D.V.; Smirnova, N.V. Interfacial Interaction in MeO<sub>x</sub>/MWNTs (Me–Cu, Ni) Nanostructures as Efficient Electrode Materials for High-Performance Supercapacitors. *Nanomaterials* **2024**, *14*, 947. [[CrossRef](#)]
19. He, X.; Zhang, N.; Shao, X.; Wu, M.; Yu, M.; Qiu, J. A layered-template-nanospace-confinement strategy for production of corrugated graphene nanosheets from petroleum pitch for supercapacitors. *Chem. Eng. J.* **2016**, *297*, 121–127. [[CrossRef](#)]
20. Balamurugan, J.; Nguyen, T.T.; Aravindan, V.; Kim, N.H.; Lee, J.H. Flexible Solid-State Asymmetric Supercapacitors Based on Nitrogen-Doped Graphene Encapsulated Ternary Metal-Nitrides with Ultralong Cycle Life. *Adv. Funct. Mater.* **2018**, *28*, e1804663. [[CrossRef](#)]
21. Kotal, M.; Kim, H.; Roy, S.; Oh, I.-K. Sulfur and nitrogen co-doped holey graphene aerogel for structurally resilient solid-state supercapacitors under high compressions. *J. Mater. Chem. A* **2017**, *5*, 17253–17266. [[CrossRef](#)]
22. Li, Q.; Guo, X.; Zhang, Y.; Zhang, W.; Ge, C.; Zhao, L.; Wang, X.; Zhang, H.; Chen, J.; Wang, Z.; et al. Porous graphene paper for supercapacitor applications. *J. Mater. Sci. Technol.* **2017**, *33*, 793–799. [[CrossRef](#)]
23. Ma, L.; Liu, R.; Niu, H.; Xing, L.; Liu, L.; Huang, Y. Flexible and Freestanding Supercapacitor Electrodes Based on Nitrogen-Doped Carbon Networks/Graphene/Bacterial Cellulose with Ultrahigh Areal Capacitance. *ACS Appl. Mater. Interfaces* **2016**, *8*, 33608–33618. [[CrossRef](#)] [[PubMed](#)]
24. Tang, X.; Zhou, H.; Cai, Z.; Cheng, D.; He, P.; Xie, P.; Zhang, D.; Fan, T. Generalized 3D Printing of Graphene-Based Mixed-Dimensional Hybrid Aerogels. *ACS Nano* **2018**, *12*, 3502–3511. [[CrossRef](#)]
25. Yu, L.; Fan, Z.; Shao, Y.; Tian, Z.; Sun, J.; Liu, Z. Versatile N-Doped MXene Ink for Printed Electrochemical Energy Storage Application. *Adv. Energy Mater.* **2019**, *9*, e1901839. [[CrossRef](#)]

26. Chen, J.; Han, Y.; Kong, X.; Deng, X.; Park, H.J.; Guo, Y.; Jin, S.; Qi, Z.; Lee, Z.; Qiao, Z.; et al. The Origin of Improved Electrical Double-Layer Capacitance by Inclusion of Topological Defects and Dopants in Graphene for Supercapacitors. *Angew. Chem. Int. Ed.* **2016**, *55*, 13822–13827. [[CrossRef](#)]
27. Mofokeng, T.P.; Tetana, Z.N.; Ozoemena, K.I. Defective 3D nitrogen-doped carbon nanotube-carbon fibre networks for high-performance supercapacitor: Transformative role of nitrogen-doping from surface-confined to diffusive kinetics. *Carbon* **2020**, *169*, 312–326. [[CrossRef](#)]
28. Qin, K.; Wang, L.; Wang, N.; Li, J.; Zhao, N.; Shi, C.; He, C.; He, F.; Ma, L.; Liu, E. Nitrogen and oxygen co-doped 3D nanoporous duct-like graphene@carbon nano-cage hybrid films for high-performance multi-style supercapacitors. *J. Mater. Chem. A* **2017**, *5*, 18535–18541. [[CrossRef](#)]
29. Kim, H.-K.; Bak, S.-M.; Lee, S.W.; Kim, M.-S.; Park, B.; Lee, S.C.; Choi, Y.J.; Jun, S.C.; Han, J.T.; Nam, K.-W.; et al. Scalable fabrication of micron-scale graphene nanomeshes for high-performance supercapacitor applications. *Energy Environ. Sci.* **2016**, *9*, 1270–1281. [[CrossRef](#)]
30. Xiang, X.; Deng, Z.; Zhang, H.; Gao, C.; Feng, S.; Liu, Z.; Liang, Q.; Fu, Y.; Liu, Y.; Liu, K. Polyaniline/Polydopamine-Regulated Nitrogen-Doped Graphene Aerogel with Well-developed Mesoporous Structure for Supercapacitor Electrode. *Chem. Eng. J.* **2023**, *477*, 147211. [[CrossRef](#)]
31. Chowdhury, S.; Balasubramanian, R. Three-dimensional graphene-based macrostructures for sustainable energy applications and climate change mitigation. *Prog. Mater. Sci.* **2017**, *90*, 224–275. [[CrossRef](#)]
32. Jiang, L.; Fan, Z. Design of advanced porous graphene materials: From graphene nanomesh to 3D architectures. *Nanoscale* **2014**, *6*, 1922–1945. [[CrossRef](#)]
33. Liu, J.; Liu, Y.; Li, P.; Wang, L.; Zhang, H.; Liu, H.; Liu, J.; Wang, Y.; Tian, W.; Wang, X.; et al. Fe-N-doped porous carbon from petroleum asphalt for highly efficient oxygen reduction reaction. *Carbon* **2018**, *126*, 1–8. [[CrossRef](#)]
34. Yang, W.; Li, R.; Jiang, B.; Wang, T.; Hou, L.; Li, Z.; Liu, Z.; Yang, F.; Li, Y. Production of hierarchical porous carbon nanosheets from cheap petroleum asphalt toward lightweight and high-performance electromagnetic wave absorbents. *Carbon* **2020**, *166*, 218–226. [[CrossRef](#)]
35. Yang, W.; Deng, B.; Hou, L.; Wang, T.; Tian, J.; Wang, S.; Li, R.; Yang, F.; Li, Y. Sulfur-fixation strategy toward controllable synthesis of molybdenum-based/carbon nanosheets derived from petroleum asphalt. *Chem. Eng. J.* **2020**, *380*, 122552. [[CrossRef](#)]
36. Cheng, B.; Yang, B.; Xie, X.; Wan, L.; Chen, J.; Du, C.; Zhang, Y.; Xie, M. Solvent-free mechanochemical synthesis of Mg-gallic acid complex for the fabrication of high-performance supercapacitor porous carbon. *Chem. Eng. J.* **2024**, *499*, 156672. [[CrossRef](#)]
37. Li, Z.Q.; Lu, C.J.; Xia, Z.P.; Zhou, Y.; Luo, Z. X-ray diffraction patterns of graphite and turbostratic carbon. *Carbon* **2007**, *45*, 1686–1695. [[CrossRef](#)]
38. Xiao, Y.-X.; Ying, J.; Tian, G.; Tao, Y.; Wei, H.; Fan, S.-Y.; Sun, Z.-H.; Zou, W.-J.; Hu, J.; Chang, G.-G.; et al. Highly dispersed PtPd on graphitic nanofibers and its heavy d- $\pi$  effect. *Appl. Catal. B-Environ.* **2019**, *259*, 118080. [[CrossRef](#)]
39. Balgis, R.; Widiyastuti, W.; Ogi, T.; Okuyama, K. Enhanced Electrocatalytic Activity of Pt/3D Hierarchical Bimodal Macroporous Carbon Nanospheres. *ACS Appl. Mater. Interfaces* **2017**, *9*, 23792–23799. [[CrossRef](#)]
40. Xiao, Y.-X.; Ying, J.; Chen, J.-B.; Dong, Y.; Yang, X.; Tian, G.; Wu, J.; Janiak, C.; Ozoemena, K.I.; Yang, X.-Y. Confined Ultrafine Pt in Porous Carbon Fibers and Their N-Enhanced Heavy d- $\pi$  Effect. *Chem. Mater.* **2022**, *34*, 3705–3714. [[CrossRef](#)]
41. Xu, J.; Wang, M.; Wickramaratne, N.P.; Jaroniec, M.; Dou, S.; Dai, L. High-performance sodium ion batteries based on a 3D anode from nitrogen-doped graphene foams. *Adv. Mater.* **2015**, *27*, 2042–2048. [[CrossRef](#)] [[PubMed](#)]
42. Kononenko, O.; Brzhezinskaya, M.; Zotov, A.; Korepanov, V.; Levashov, V.; Matveev, V.; Roshchupkin, D. Influence of numerous Moiré superlattices on transport properties of twisted multilayer graphene. *Carbon* **2022**, *194*, 52–61. [[CrossRef](#)]
43. Liu, X.; Choi, J.; Xu, Z.; Gery, C.P.; Fleischmann, S.; Forse, A.C. Raman Spectroscopy Measurements Support Disorder-Driven Capacitance in Nanoporous Carbons. *J. Am. Chem. Soc.* **2024**; *accepted*. [[CrossRef](#)] [[PubMed](#)]
44. Chen, L.; Zhang, Y.; Lin, C.; Yang, W.; Meng, Y.; Guo, Y.; Li, M.; Xiao, D. Hierarchically porous nitrogen-rich carbon derived from wheat straw as an ultra-high-rate anode for lithium ion batteries. *J. Mater. Chem. A* **2014**, *2*, 9684–9690. [[CrossRef](#)]
45. Dong, Y.; Chen, J.-B.; Ying, J.; Xiao, Y.-X.; Tian, G.; Symes, M.D.; Yang, X.-Y. Efficient Water Dissociation on Confined Ultrafine Pt via Pyridinic N-Enhanced Heavy d- $\pi$  Interaction. *Chem. Mater.* **2022**, *34*, 8271–8279. [[CrossRef](#)]
46. Rabchinskii, M.; Ryzhkov, S.A.; Gudkov, M.V.; Baidakova, M.V.; Saveliev, S.D.; Pavlov, S.I.; Shnitov, V.V.; Kirilenko, D.A.; Stolyarova, D.Y.; Lebedev, A.M.; et al. Unveiling a facile approach for large-scale synthesis of N-doped graphene with tuned electrical properties. *2D Mater.* **2020**, *7*, 045001. [[CrossRef](#)]
47. Brzhezinskaya, M.; Mishakov, I.V.; Bauman, Y.I.; Shubin, Y.V.; Maksimova, T.A.; Stoyanovskii, V.O.; Gerasimov, E.Y.; Vedyagin, A.A. One-pot functionalization of catalytically derived carbon nanostructures with heteroatoms for toxic-free environment. *Appl. Surf. Sci.* **2022**, *590*, 153055. [[CrossRef](#)]
48. Bulushev, D.A.; Zacharska, M.; Shlyakhova, E.V.; Chuvilin, A.L.; Gao, Y.; Beloshapkin, S.; Okotrub, A.V.; Bulusheva, L.G. Single Isolated Pd<sup>2+</sup> Cations Supported on N-Doped Carbon as Active Sites for Hydrogen Production from Formic Acid Decomposition. *ACS Catal.* **2016**, *6*, 681–691. [[CrossRef](#)]
49. Khazaali, A.; Godbille-Cardona, G.; Barz, D.P.J. A Novel Flexible Hybrid Battery–Supercapacitor Based on a Self-Assembled Vanadium-Graphene Hydrogel. *Adv. Funct. Mater.* **2020**, *30*, 1910738. [[CrossRef](#)]
50. Liu, Z.; Duan, C.; Dou, S.; Yuan, Q.; Xu, J.; Liu, W.D.; Chen, Y. Ultrafast Porous Carbon Activation Promises High-Energy Density Supercapacitors. *Small* **2022**, *18*, e2200954. [[CrossRef](#)]

51. Tian, W.; Zhang, H.; Sun, H.; Tadé, M.O.; Wang, S. Template-free synthesis of N-doped carbon with pillared-layered pores as bifunctional materials for supercapacitor and environmental applications. *Carbon* **2017**, *118*, 98–105. [[CrossRef](#)]
52. Zhang, F.; Liu, T.; Hou, G.; Kou, T.; Yue, L.; Guan, R.; Li, Y. Hierarchically porous carbon foams for electric double layer capacitors. *Nano Res.* **2016**, *9*, 2875–2888. [[CrossRef](#)]
53. Qie, L.; Chen, W.; Wang, Z.; Shao, Q.; Li, X.; Yuan, L.; Hu, X.; Zhang, W.; Huang, Y. Nitrogen-Doped Porous Carbon Nanofiber Webs as Anodes for Lithium Ion Batteries with a Superhigh Capacity and Rate Capability. *Adv. Mater.* **2012**, *24*, 2047–2050. [[CrossRef](#)] [[PubMed](#)]

**Disclaimer/Publisher’s Note:** The statements, opinions and data contained in all publications are solely those of the individual author(s) and contributor(s) and not of MDPI and/or the editor(s). MDPI and/or the editor(s) disclaim responsibility for any injury to people or property resulting from any ideas, methods, instructions or products referred to in the content.